Published in final edited form as:
Int J Remote Sens. 2018 January 29; 39(9): 2818–2846. doi:10.1080/01431161.2018.1430912.

Monitoring Algal Blooms in drinking water reservoirs using the Landsat 8 Operational Land Imager

Darryl Keith[1], **Jennifer Rover**[2], **Jason Green**[3], **Brian Zalewsky**[4], **Mike Charpentier**[5], **Glen Thursby**[1], and **Joseph Bishop**[1]

[1]United States Environmental Protection Agency, Atlantic Ecology Division, Narragansett, Rhode Island 02882, USA.

[2]United States Geological Survey, Earth Resources Observation and Science Center, Sioux Falls, South Dakota 57198-0001, USA.

[3]Intensive Survey Branch, North Carolina Department of Environmental and Natural Resources; North Carolina Department of Environmental Quality; Raleigh, North Carolina 27699-1623, USA.

[4]Rhode Island Department of Environmental Management, Providence, Rhode Island 02908, USA.

[5]Raytheon Company, Narragansett, Rhode Island 02882, USA.

Abstract

In this study, we demonstrated that the Landsat-8 Operational Land Imager (OLI) sensor is a powerful tool that can provide periodic and system-wide information on the condition of drinking water reservoirs. The OLI is a multispectral radiometer (30 m spatial resolution) that allows ecosystem observations at spatial and temporal scales that allow the environmental community and water managers another means to monitor changes in water quality not feasible with field-based monitoring. Using the provisional Land Surface Reflectance (LSR) product and field-collected chlorophyll-*a* (chl-*a*) concentrations from drinking water monitoring programs in North Carolina and Rhode Island, we compared five established approaches for estimating chl-*a* concentrations using spectral data. We found that using the 3 band reflectance approach with a combination of OLI spectral bands 1, 3, and 5, produced the most promising results for accurately estimating chl-*a* concentrations in lakes (R^2 value of 0.66; RMSE value of 8.9 μg l^{-1}). Using this model, we forecast the spatial and temporal variability of chl-*a* for Jordan Lake, a recreational and drinking water source in piedmont North Carolina and several small ponds that supply drinking water in southeastern Rhode Island.

Keywords

Landsat-8; chlorophyll-*a*; water quality; monitoring

corresponding author; keith.darryl@epa.gov; thursby.glen@epa.gov; bishop.joseph@epa.gov.

1. Introduction

The US Environmental Protection Agency (USEPA) estimates that between 30 and 50 million people in the United States use drinking water from lakes and reservoirs that may be vulnerable to algal blooms that cause human and animal health risks, anoxia and fish kills, and taste and odor issues. Typically, algal blooms occur in eutrophic or hypereutrophic waters in association with elevated levels of nitrogen and phosphorus (Ohio EPA, 2013). Freshwater algal blooms consist of phytoplankton (composed of green algae and cyanobacteria) which contain chlorophyll-*a* (chl-*a*), a spectrally active compound that is commonly used as a key indicator of water quality (Reif, 2011; Mishra and Mishra, 2012), a proxy for biomass (Vos et al., 1986; Wynne et al., 2012; Keith et al., 2014; Kudela et al., 2015) and as a human health guideline for cyanobacteria monitoring (WHO, 2003). Some blooms are classified as harmful algal blooms (HABs) due to the release of toxins (Ohio EPA, 2013). HABs are a global problem that have been implicated in human and animal illness and death in more than 45 countries (Graham, 2006).

There are 16.9 million hectares of lakes, ponds, and reservoirs in the United States of which 6.5 million hectares (39%) are assessed by state agencies (USEPA, 2009). Of the lakes that were assessed, 4.2 million hectares (64%) were identified as impaired or not supporting one or more of their designated uses such as fishing or swimming (USEPA, 2009). Leading causes of impairment were nutrients, metals, sewage, sedimentation, and nuisance species. The USEPA has estimated that approximately 769,000 hectares (25%) of lakes, reservoirs, and ponds have poor water quality because of nitrogen and phosphorus pollution (USEPA, 2009). Economically, the increased frequency and duration of algal blooms, particularly during warm months, has resulted not only in increased costs associated with drinking water treatment but also impacts on tourism, real estate values, commercial fishing and recreational uses.

An effective method for monitoring algal blooms and HABs in coastal and offshore waters is to derive chl-*a* concentrations from remotely sensed spectral data (Schalles et al., 1998; Keith, 2010; Klemas, 2012) based on the optical properties of these waters. For HAB monitoring, chl-*a* is the preferred pigment because most existing satellite imagers are better suited to capture the chl-*a* reflectance peak in the near-infrared (NIR) region of the visible spectrum than the narrow peak at 620 nm, which is associated with phycocyanin, the pigment diagnostic of freshwater cyanobacteria (also known as blue-green algae).

The objective of this study was to use spectral data generated by the Landsat-8 OLI sensor to estimate algal biomass in inland lakes and reservoirs from Land Surface Reflectance (LSR) imagery using a reflectance based algorithm. The goals of this study were to: 1) retrieve atmospherically and sun-glint corrected spectral reflectance signatures of chl-*a* laden reservoir and lake waters from Jordan Lake, a temperate reservoir in central North Carolina, and several small drinking water reservoirs in southeastern Rhode Island; 2) identify several published approaches that have previously retrieved chl-*a* concentrations from inland water bodies using spectral data from Landsat-7 and Landsat-8; 3) assess and validate the performance of these approaches against laboratory measured chl-*a* datasets from field collected sampling using statistical measures; and 4) use the best performing algorithm to

predict algal biomass and map the spatial and temporal variability of chlorophyll-*a* within Jordan Lake and the Rhode Island ponds and reservoirs.

2. Methods

2.1 Study Areas

B. Everett Jordan Lake is a man-made lake located in the largest watershed in North Carolina to provide ecosystem services such as flood control from hurricanes, recreational areas, and fish and wildlife habitat. Jordan Lake has a surface area of 5,625 hectares and drains approximately 4,367 km^2 from 10 surrounding counties (Figure 1; NCDENR, 2014). Jordan Lake serves also as a drinking water reservoir (Jordan Lake Reservoir) for the rapidly growing greater Raleigh-Durham (North Carolina) regional area (population > 2 million) that has historically been one of the most eutrophic reservoirs in North Carolina. The eutrophic nature of the reservoir is linked to excessive nitrogen and phosphorous loading from both point (wastewater treatment plants) and non-point (housing developments, farmlands, stormwater runoff) sources in the watershed (NCDENR, 2014). Point sources contribute an average of 6,803,885 kg of nitrogen and 63,503 kg of phosphorus to the reservoir annually. Non-point sources contribute an average of 11,339,809 kg of nitrogen and 158,757 kg of phosphorus annually to the reservoir (NCDENR, 2007).

In southeastern Rhode Island (RI), nine surface water bodies which are interconnected through a complex network of piping and pump stations, referred to as the Newport Water Supply, serve as drinking water reservoirs to a population of approximately 70, 000 (Figure 2). These coastal plain ponds supply 60,567 m^3 day^{-1} of drinking water to the city of Newport, which is urban, and the towns of Middletown and Portsmouth (Rhode Island) which are historically farming communities that are presently undergoing urbanization (Town of Portsmouth, RI, 2002).

The major threat to the water quality of the reservoirs is the nature of land use and non-point pollution within the watershed (Town of Portsmouth, RI, 2002). Monitoring by the Rhode Island Department of Environmental Management (RIDEM) has shown that all nine water bodies exhibit eutrophic conditions due to moderately to severely elevated phosphorous and nitrogen concentrations resulting in violations of aquatic life use criteria, excessive algal growth and frequent cyanobacteria blooms (RIDEM, 2015). Additionally, the RI Department of Health (RI DOH) has determined that these reservoirs should be listed on the Clean Water Act 303d list of impaired waters due to excessive algal growth, which has resulted in elevated levels of Total Organic Carbon (TOC) at the intake of water treatment plants on Lawton Valley Pond and Green End Pond (Figure 2).

2.2 Field Sampling

In situ data were provided by the Division of Water Quality (DWQ) at the North Carolina Department of Environmental Quality and Natural Resources (NCDENR) and RIDEM.

DWQ routinely collects surface water quality data at 9 sites within Jordan Lake (Figure 1) in support of water quality monitoring (NCDENR, 2014). During the period of this study, 11 more monitoring sites were added to the monitoring plan to support a demonstration project

sponsored by NCDENR, per 2013 NC legislative directive. For samples collected at the 20 sites, field collection followed State approved Standard Operating Procedures as included in the Ambient Lakes Monitoring Program (ALMP) Quality Assurance Project Plan Version 2.0 (March 2014). Chl-*a* samples were processed according to EPA Method 445 (Modified Option) (Arar and Collins, 1997).

Newport Water Supply locations were sampled biweekly from early May through October 2015 by field crews from RIDEM following State approved Standard Operating Procedures as included in the 2015 Sample Plan for RIDEM Water Quality Monitoring in the Newport Reservoirs (Figure 2; RIDEM, 2015). Each reservoir was sampled at a single location above its deepest point based on existing bathymetric data (RIDEM, 2015). Water samples were collected at the surface, mid-depth, and bottom for a variety of parameters (e.g., nitrogen, dissolved organic carbon, total phosphorus, orthophosphate) with surface water samples collected for chl-*a* concentrations. Samples were analyzed according to US EPA Atlantic Ecology Division (AED) Operating Procedure "Non-Acid Determination of Chlorophyll-*a* Using a Turner Designs AU-10 Fluorometer" (LOP-AED/WDB/GBT/2015-01-00), which is based on EPA Method 445.0 (Arar and Collins, 1997).

2.3 Landsat-8 image processing

Landsat-8 (L8) Land Surface Reflectance (LSR) images were accessed from the Landsat archive at the US Geological Survey (USGS) Earth Resources Observation and Science (EROS) Center using the EarthExplorer (EE; http://earthexplorer.usgs.gov) client/server interface (USGS, 2016). This study used images processed using LSR version 0.3.1 to retrieve surface reflection data and these output products are provisional (USGS, 2016). Constraints on processing Landsat-8 LSR include hyper-arid or snow covered regions, scenes with low sun angle conditions (sun angles < 14°), coastal regions where land area is small relative to adjacent water, and areas with extensive cloud contamination (USGS, 2016). LSR output contained: surface reflectance data files (bands 1–7), Cloud QA band (sr_cloud), Interpolation Flag QA band (sr_ipflag), CFmask (sr_cfmask), CFmask cloud confidence band (sr_cfmask_conf), and surface reflectance metadata file (.xml). Filenames utilized the original sceneID followed by "_sr_," for example, "LC82330132014265LGN00_sr_*" (USGS, 2016).

Generally, OLI data are nominally processed using the Level 1 Product Generation System (LPGS) into 185 km × 180 km Level 1 terrain-corrected (L1T) products that have a typical 950 MB compressed GeoTiff file. OLI spectral bands are stored as geo-located 16-bit digital numbers (DN). An associated metadata file stores spectral band gain and offset numbers that can be used to linearly convert the digital numbers to top-of-the-atmosphere radiance (W m $^{-2}$ sr^{-1} μm^{-1}) and to convert the OLI digital numbers to at-sensor reflectance (unitless). The Landsat 8 L1T data processing includes radiometric calibration, systematic geometric correction, precision correction assisted by ground control chips, and the use of a digital elevation model to correct parallax error due to local topographic relief (Lee et al., 2004; Storey et al., 2008). The LSR data used in this study were generated from the provisional Landsat-8 Surface Reflectance (L8SR) algorithm, which is a specialized software originally developed at the NASA Goddard Space Flight Center (GSFC) to convert top-of-the-

atmosphere (TOA) L1T spectral radiances to TOA reflectance. The LSR product is generated at 30-meter spatial resolution on a Universal Transverse Mercator (UTM) or Polar Stereographic (PS) mapping grid. The default file format is GeoTIFF, but options for delivery in Hierarchical Data Format – Earth Observing System – 2 (HDF-EOS-2; *.hdf), or ENVI binary (*.img) are available (USGS, 2016). LSR products are available for Landsat-8 scenes beginning from April 2013 to within one week of most recent acquisition.

During L8 LSR processing, atmospheric correction is conducted using a USGS algorithm for radiative transfer modelling. Aerosol correction is accomplished using the "sr_cloud" band. The sr_cloud band is used to determine cloud presence as well as the level of surface reflectance correction needed as determined from aerosol levels. For land pixels, aerosol levels are classified according to values in the Cloud QA band. Water pixels are routinely flagged and removed from further processing (USGS, 2016).

Landsat-8 LSR images were retrieved using procedures in the Surface Reflectance product guide (USGS, 2016). Initially, images were identified by Path 16, Row 35, (North Carolina) and Path 12, Row 31 (Rhode Island and southeastern Massachusetts) and browsed by date range (Table 1). For algorithm development and evaluation, 11 LSR images (and metadata) from May 2013 to September 2014 (for Jordan Lake) and May 2015 to August 2015 (for Rhode Island reservoirs) were downloaded and saved in the default GeoTIFF format for OLI bands 1 – 6.

2.4 Image Processing

A key challenge in retrieving accurate satellite-based measurements is the removal of unwanted contributions to reflectance from water pixels due to atmospheric effects. The steps for atmospherically correcting Landsat-8 images for aerosol scattering were based on the theory that reflectance (ρ) at the top of the atmosphere (TOA) could be derived from TOA radiance measured by a satellite sensor (Gordon and Wang, 1994):

$$\rho_{\mathrm{TOA}} = (\pi L)/(F_0 \cos\theta_0) \quad \text{Equation (1)}$$

where L is the upward radiance from the earth surface, F_0 is the extraterrestrial solar irradiance, and θ_0 is the solar zenith angle (Vanhellemont and Ruddick, 2015). The TOA reflectance (ρ_{TOA}) could be written as:

$$\rho_{\mathrm{TOA}} = \rho_{\mathrm{r}} + \rho_{\mathrm{A}} + t\rho_{\mathrm{w}} \quad \text{Equation (2)}$$

where ρ_{TOA} is the total reflectance measured at the top of the atmosphere, ρ_{r} is the reflectance resulting from multiple scattering by air molecules (Rayleigh scattering) in the absence of aerosols, ρ_{A} is the reflectance resulting from multiple scattering by aerosols in the absence of air, t is the diffuse transmittance of the atmosphere, and ρ_{w} is the water-leaving reflectance just above the surface. The purpose of atmospherically correcting an image is to retrieve ρ_{w}.

The Rayleigh-corrected reflectance values of water pixels (ρ_{LSR})water pixels in the Landsat-8 LSR images were represented as:

$$(\rho_{LSR})_{\text{water pixels}} = \rho_{TOA} - \rho_r \quad \text{Equation (3)}$$

Equation 3 could then be rewritten to reflect that water pixels in the LSR product still contained aerosol and water-leaving reflectance contributions:

$$(\rho_{LSR})_{\text{water pixels}} = \rho_A + t\rho_w \quad \text{Equation (4)}$$

Because the OLI is an instrument designed for land-based studies, the sensor was not equipped with the appropriate bands required by traditional water-based atmospheric correction algorithms. The general approach for water-based atmospheric correction is to use spectral bands for which ρ_w is known to make an assessment of the aerosol contribution (Gordon and Wang, 1994). The most widely-used technique to retrieve aerosol reflectance over water pixels and correct satellite imagery based on the assumption that ρ_w in the NIR (700 nm < λ < 1000 nm, where λ equals wavelength) is negligible. For open ocean pixels the assumption was that any reflectance signal observed in this spectral region is solely due to atmospheric effects and is an indicator of aerosol contribution to all wavelengths (Emberton et al., 2016; Gordon and Wang, 1994). However, this assumption does not hold for coastal and lake waters as moderate - high concentrations of suspended particles characteristically produce appreciable scattering and non-zero contributions to the water leaving signal at the NIR bands (Vanhellemont and Ruddick, 2015; Mobley, 2015; Knaeps et al., 2012; Wang and Shi, 2005; Ruddick et al., 2000; Siegel et al., 2000; Stumpf et al., 2003). In these instances, the approach would lead to overestimation of $\rho_A(\lambda)$ in the NIR region as particle scattering from surface waters would be treated as if it were atmospheric aerosol scattering. The overestimation of atmospheric effects would result in very low, possibly negative $\rho_w(\lambda)$ values at short wavelengths in the visible region (Ruddick et al., 2000; Moses et al., 2009). We found that the water leaving signal at the NIR band (band 5) contained appreciable scattering and non-zero contributions, which were characteristic in Landsat-8 images in this study.

This problem required using the short-wave infrared wavelengths (SWIR) for atmosphere correction (Vanhellemont and Ruddick, 2015; Wang and Shi, 2005). The use of SWIR bands for atmosphere correction is not commonplace because not many ocean color sensors have SWIR bands and existing SWIR bands often have significant noise levels (Vanhellemont and Ruddick, 2015). The major assumption of using SWIR wavelengths is $\rho_w(\lambda)$ is virtually zero (i.e., black), even for turbid water, due to the high absorption of water in this spectral region (Kou et al., 1993; Pope and Fry, 1997). As such, any signal in this region is assumed to be solely due to atmospheric effects. This assumption has been shown to be mostly valid at the shorter SWIR wavelengths (up to 1240 nm) for turbid marine waters (Emberton et al., 2016; Li et al., 2003). However, non-zero reflectances have been observed at wavelengths λ < 1.6 μm in extremely turbid estuarine, lake and river waters (Knaeps et al., 2012; Wang et

al., 2011; Shi and Wang, 2009a). At the longer SWIR wavelengths (λ > 1.6 μm), Shi and Wang (2009a) reported that even extremely turbid waters were effectively black. Currently there is no generic processing method for the retrieval of $\rho_A(\lambda)$ using bands from 1.0 μm < λ < 3.0 μm; however, several approaches have successfully demonstrated the value of using the SWIR wavelengths as a means to improve ocean color products from turbid coastal waters measured by the MODIS-Aqua sensor (Wang, 2007; Wang et al. 2007; Shi and Wang, 2009a). Gerace and Schott (2012) and Concha and Schott (2016) have developed atmospheric correction routines for the OLI that incorporated the dark pixel assumption and used the ratio of NIR/SWIR reflectance to create a Look-Up Table (LUT) from which an atmosphere could be chosen to estimate the spectral reflectance due to water column.

In the following steps, OLI LSR data were processed using Microsoft Excel to correct for aerosol scattering and retrieve remotely sensed reflectance.

- Step 1: Sun elevation data in the header file was used to determine the solar zenith angle (θs).

$$\theta_s = 90° - \text{sun elevation} \quad \text{Equation (5)}$$

- Step 2: Obtain Rayleigh coefficients (τ) for the OLI (Franz et al. 2015, Table 2).
- Step 3: Derive the atmospheric diffuse transmission ($t_0(\lambda)$) from Sun to surface for each band using:

$$t_0(\lambda) = \exp(-0.5\tau/\cos\theta_s) \quad \text{Equation (6)}$$

- Step 4: LSR digital values were converted into reflectance (unitless) by dividing by 10,000 (Step 4).
- Step 5: Use reflectance in OLI band 6 to identify land and cloud pixels and remove when values were greater than 0.0215 (Vanhellemont and Ruddick, 2015; Vanhellemont and Ruddick, 2014a).

In Steps 6 – 10, Landsat-8 water pixels were atmospherically corrected for aerosol reflectance to retrieve water-leaving reflectance using the OLI near Infrared (NIR; band 5) and short-wave infrared (SWIR; band 6) bands based on the VIR-SWIR atmospheric correction method (Vanhellemont and Ruddick, 2015).

- Step 6: Aerosol type (ε) was determined from the ratio of band 6 to band 5 reflectance ($\varepsilon^{6,5}$) for each pixel over water.
- Step 7: If it is assumed that the aerosol type is constant across the image then the median value of $\varepsilon^{6,5}$ from pixels derived in Step 6 is used for additional processing. Otherwise, the image was processed using individual $\varepsilon^{6,5}$ values.
- Step 8: The spectral ε for each band (λ_i) is derived from (Gordon and Wang, 1994):

$$\varepsilon^{i,\mathrm{L}} = (\varepsilon^{\mathrm{S,L}})^{\sigma i} \quad \text{Equation (7)}$$

$$\text{where } \sigma_{\mathrm{i}} = (\lambda_{\mathrm{L}} - \lambda_{\mathrm{i}})/(\lambda_{\mathrm{L}} - \lambda_{\mathrm{S}}) \quad \text{Equation (8)}$$

L = 1.610 μm, the longest wavelength used

S = 0.443 μm, the shortest wavelength used

- Step 9: Derive water leaving reflectance (ρ_{w}) values for each band (ρ^{i}):

$$\rho_{\mathrm{w}}(\lambda) = 1/t_0(\lambda)\rho^{\mathrm{i}} - ((\varepsilon^{\mathrm{i},6})\rho(\text{band } 6)) \quad \text{Equation (9)}$$

where ($\varepsilon^{\mathrm{i},6}$) = spectral aerosol type at each band i and band 6

ρ^{i} = the pixel reflectance at band i

- Step 10: Remote sensing reflectance (R_{rs}) was calculated using Hu et al. (2004)

$$R_{\mathrm{rs}}(\lambda) = \rho_{\mathrm{w}}(\lambda)/(\pi/t_0(\lambda)) \quad \text{Equation (10)}$$

In order to demonstrate that the atmospheric correction of OLI data for aerosols provided an added-value to the estimation of chl-*a* concentrations, the percent difference of chl-*a* derived from spectral data corrected for aerosols and those corrected only for Rayleigh scattering was used as a metric for comparison. The percent difference was determined from:

$$\text{difference} = ((\mathrm{V}_1 - \mathrm{V}_2)/((\mathrm{V}_1 + \mathrm{V}_2/2))) \times 100\% \quad \text{Equation (11)}$$

where:

V_1 = chl-*a* derived from pixels corrected for Rayleigh atmospheric effects

V_2 = chl-*a* derived from pixels corrected for Rayleigh and Aerosol atmospheric effects

2.5 Sun-glint Removal

An additional challenge in retrieving accurate satellite-based measurements based on the spectral characteristics of water bodies is the removal of unwanted reflectance contributions to the signal due to sun-glint effects. Sun-glint occurs when sunlight reflects off the surface of the water into the field of view of the sensor (Cox and Munk, 1954; Wang and Bailey, 2001; Zhang and Wang, 2010). For push-broom sensors like the OLI, Mustard et al. (2002) and Dekker et al. (2013) recommended that, in order to avoid sun-glint problems, solar zenith angles be constrained to angles between 30° – 60°.

Several approaches have been proposed for the detection of sun-glint including labelling high ρ_w values as contaminated (Hooker et al., 2002); calculating the ratio between bright and dark pixels through histogram analysis (Garaba and Zielinski, 2013); spectral matching; and directly computing sun-glint contributions from total radiances and Rayleigh corrected radiances (Shanmugan, 2012). However, the Landsat-8 OLI is not equipped with the appropriate wavelengths in the red and infrared regions required by many glint correction algorithms.

Using the recommended criteria for solar zenith angles, a sun-glint correction was applied for those images whose solar zenith angles were less than 30°. During image processing, each pixel was corrected for sun-glint using the approach of Hochberg et al., 2003 and revised by Hedley et al., 2005.

The major assumptions of the Hochberg et al. (2003) approach are that: 1) water was strongly absorbing at the near-infrared (NIR) wavelengths and that any signals represent sun-glint reflected from the sea surface and a spatially constant 'ambient' NIR component, 2) the amount of sun-glint in the visible bands was linearly related, using regression analysis, to the brightness of the NIR band and visible bands (Hedley et al., 2005; Hochberg et al., 2003), and 3) sun-glint effects could be removed by subtracting reflectance from a "glint free or clear water" pixel (i.e. the pixel with the lowest NIR value) (Wicaksono, 2012).

To correct for sun-glint at each band, the approach of Hedley et al. (2005) was used to remove glint effects for Landsat-8 images with zenith angles less than 30°. An additional assumption of this approach is that a linear relationship exists between NIR reflection brightness and amount of sun-glint in the visible bands (Hochberg et al., 2003). In the Hedley et al. (2005) method, glint effects were removed from image pixels using the reflectance (ρ) brightness for each visible (VIS) band (i) ($\rho_{i(\mathrm{VIS})}$) and the brightness of the NIR band ($\rho_{(\mathrm{NIR})}$). $\rho_{i(\mathrm{VIS})}$ is defined as the reflectance of the ith visible band. Linear regression of a subset of image pixels was used to establish the relationship between $\rho_{(\mathrm{NIR})}$ and $\rho_{i(\mathrm{VIS})}$ for each band. The slope (m) of the regression equation at each ith visible band was used to derive band reflectance corrected for sun-glint effects ($\rho(\lambda)'$) according to:

$$\rho(\lambda)' = \rho_{i(\mathrm{VIS})} - m_i(\rho_{(\mathrm{NIR})} - \rho_{\min(\mathrm{NIR})}) \quad \text{Equation (12)}$$

where $\rho_{\min(\mathrm{NIR})}$ represented the NIR brightness of a pixel (i.e., a clear water pixel) with no sun glint and estimated from the minimum OLI band 5 reflectance found in the subset of pixels used in the regression.

The importance of identifying the clear water pixels is critical as the third assumption may not hold valid for coastal or inland reservoir and recreational waters.

2.6 Algorithm Development

Since sampling locations were georeferenced, it was possible to compare matchups between field data and corresponding Landsat-8 pixels to assess the published predictive chl-*a* algorithms. In this study, we applied the geometrically and radiometrically corrected R_{rs} data

to five established reflectance-based approaches to derive chl-*a* and to assess their feasibility to accurately estimate chl-*a* in CDOM dominated, turbid productive lake waters and drinking water reservoirs. The model/approaches consisted of a simple three band reflectance model (Dall'Olmo et al., 2003), a blue-green band reflectance model (Gordon and Morel, 1983), a green-blue reflectance model (Turner, 2010), and two four band reflectance models (Fluorescence Line Height (FLH) Blue and Violet models, Beck et al., 2016).

Model coefficients were determined using model I linear regression analysis based on a subset of Landsat-8 spectral data and laboratory measured chl-*a* values from 20 stations in North Carolina and Rhode Island covering 2013 – 2015 (Table 3). Because NCDENR and RIDEM field sampling dates were not specifically timed to coincide with L-8 overpass times, the difference between the field and satellite datasets varied from same day to 4 days post-overflight. Regressions relationships were graphically illustrated.

2.7 Algorithm Validation

The prediction quality of the developed models was validated using model II linear regression analysis (i.e., major axis method) with the goal of estimating the relationship between chlorophyll predicted from L-8 images and laboratory measured chl-*a* to derive Pearson's correlation coefficient (r) as well as the coefficient of determination (R^2). We also used root-mean-square error (RMSE), Mean Absolute Error (MAE) and Mean Absolute Percent Error (MAPE) of laboratory measured and model predicted chl-*a*. Predicted values were adjusted for bias using the Normalized Forecast Metric (NFM). Note that the Landsat-8 R_{rs} pixel values used to evaluate the effectiveness of the models were not the same as those used to construct the models.

The best performing algorithm was used to predict chl-*a* concentrations and map the spatial distribution of algal biomass within Jordan Lake for Autumn 2014 though Spring 2015 and as a synoptic view of Newport Water Supply ponds and reservoirs in late Summer 2015. Chlorophyll-*a* concentrations for each image were mapped using the nearest neighbor resampling method in SeaDAS Version 7.4.

Models were validated using predicted chl-*a* values and extracted chl-*a* from 15 stations in Jordan Lake and Rhode Island which were not used to derive model coefficients (Table 4). The Landsat 8 locations used for validation were centered at the latitude and longitude locations of field stations. Chlorophyll-*a* concentrations ranged from 24 -72 μg l^{-1} in Jordan Lake and 6 to 147 μg l^{-1} in the Newport Water Supply ponds. Samples were collected either on the same day or within two days of a Landsat-8 overpass (Table 4).

3. Results and Discussion

3.1 Landsat-8 Image Processing

Landsat-8 images from North Carolina and Rhode Island were atmospherically corrected for aerosol scattering using the OLI SWIR (band 6) and NIR (band 5) for sun glint removal. Landsat-8 image LC80160352014137LGN00_sr from Jordan Lake is an example of the change in the magnitude of reflectance from the aerosol correction and sun-glint removal processes resulting in the retrieval of remote sensing reflectance (Figure 3).

3.2 Sun-glint Removal

As indicated previously, we observed that Landsat-8 NIR (band 5) contained significant reflectance values in all images that could be due to backscatter from suspended sediments (e.g., Doxaran et al., 2002) and floating algae (Hu, 2009).

Figure 3 also shows an example of the effect of the sun-glint correction on SWIR corrected reflectance data using image LC80160352014137LGN00_sr (solar zenith angle = 24.2°) from Jordan Lake.

3.3 Typology of Jordan Lake and RI Ponds Based on Remotely Sensed Reflectance

Phytoplankton productivity in open and coastal ocean and estuarine environments is often inferred from the shape of the visible spectra observed by earth orbiting sensors. Spectral variation can therefore be used to identify constituents in the water column. The shape and magnitude of the remotely sensed spectra are due to variability in the inherent optical properties (IOPs) of these waters which are influenced by regional geology, land use, land cover, and nutrient concentrations in the water column.

From the reflectance properties of 44 lakes in the Adirondack mountain region of New York State, Vertucci and Likens (1989) described five distinct types of reflectance spectra and demonstrated that small changes in concentration of plant pigments, dissolved organic carbon (DOC) and suspended material changed the relationships between reflectance and water quality.

In this study, R_{rs} values for OLI bands 1 – 6 were averaged for each image to create a general spectral curve. The averaged spectral curves were compiled to graphically illustrate the variability observed between remotely sensed reflectance spectra within the L-8 images used in this study (Figure 4a and 4b). It should be noted that these spectra have not been corrected for mixed pixel effects or the effects that bottom reflectance and adjacency to land can have on the water leaving signal.

In general, these curves show that Jordan Lake and the Newport ponds commonly exhibit prominent reflectance peaks in the OLI green band (band 3: 530-590 nm). Jordan Lake, three images had spectra which were reflective in the OLI NIR band (band 5: 850-880 nm) (Figure 4a). The Newport drinking water ponds showed two sites with spectra which were reflective in the (Figure 4b). Similar peaks in the NIR have also been observed in Terra and Aqua MODIS, HJ-1, and Landsat-5 and 7 coastal and open ocean images and were associated with macroalgae floating on the water surface (Xing and Hu, 2016; Hu, 2009).

For both locations, reflectance was usually low in the OLI coastal (band 1: 430-450 nm) and blue (band 2: 450-510 nm) bands, due to CDOM and chl-*a* absorption. A reflectance minima was also observed in the OLI red band (band 4: 640-670 nm).

When the spectra in Figure 4 are compared to the spectral classification scheme of Vertucci and Likens (1989), the Jordan Lake and Newport drinking water ponds R_{rs} spectra were very similar their Type 3 spectra. Type 3 spectra were characterized by maximum reflectance between 550-575 nm with reflectance values that declined sharply at wavelengths on each

side of the maximum. Vertucci and Likens (1989) indicated that this spectral type was characteristic of lakes that were green in color with varying water clarity.

3.4 Reflectance Band-ratio Algorithms

We conducted a review of the scientific literature in order to understand the optical character of freshwater environments and how inherent optical properties such as coloured dissolved organic matter (CDOM), non-algal particle (NAP), water, and phytoplankton absorptions matchup with the position of Landsat-8 OLI visible bands. We found such studies were rare, with the exception of Thrane et al. (2014) which used the inherent optical properties of 75 large lakes in Norway and Sweden to derive a bio-optical model to estimate primary production in boreal lakes. Using this optical dataset, the OLI visible bands, located around their center bandwidths (Table 2), were overlain onto phytoplankton, CDOM, NAP, and water absorption curves generated by Thrane et al. (Figure 5).

Using the spectral curves of the Thrane et al. optical datasets as a frame of reference, we overlaid the bandwidth positions of the OLI bands onto the absorption characteristics of these waters. In terms of phytoplankton absorption, chlorophyll absorption peaks coincide with bands 1 and 2. Bands 3 and 4 coincide with areas of absorption minima (Figure 5a). Not unexpectedly, CDOM would be the dominant absorber of light in OLI bands 1-3 (Figure 5b). Characteristically, CDOM absorption rapidly declines across band 4 approaching zero in the red spectral region (Figure 5b). The curves also show that NAP absorption reached average maximum values within the bandwidth of OLI band 2, although several boreal lakes showed maximum absorptions in OLI band 3 (Figure 5c). Finally, water absorption has negligible impact in OLI bands 1-3 but is the dominant light absorber in red portion (band 4) of the spectrum.

From a spectrophotometric perspective, OLI band 1 is positioned to capture the chl-*a* absorption peak at 430 nm in the violet-blue portion of the spectrum (Rabinowitch and Govinjee, 1969; Jeffrey et al., 1997). OLI band 2 is positioned to capture the chl-*b* absorption peak at 480 nm in the blue-green portion of the spectrum (a locally oxidized derivative of chlorophyll-*a*, (Rabinowitch and Govinjee, 1969; Jeffrey et al., 1997). OLI band 3 is positioned to capture the phycoerythin peak at 562 nm (Lemasson et al., 1973; Poryvkina et al., 2000). OLI band 4 (640-670 nm) is positioned to capture secondary chl-*b* absorption at 650 nm in the red portion of the spectrum (Jeffrey et al., 1997) but not centered to retrieve chl-*a* absorption between 670-680 nm.

Coefficients for the algorithms developed in this study were determined using linear regression of band ratios and laboratory measured chl-*a* values from 19 stations in Jordan Lake and Rhode Island centered at the latitude and longitude of field samples (Table 6). Chl-*a* concentrations ranged from a minimum of 6 to 147 $\mu g\ l^{-1}$. Samples were collected on the day of a Landsat 8 overpass or within 4 days of the sensor overflight.

3.4.1 Three-band reflectance models—The three-band reflectance model of Gitleson et al. (2009) and Dall'Olmo et al. (2003) used change in the reflectance spectrum at different wavelengths to quantify chlorophyll absorption by spectral difference (Blondeau-Patissier et

al., 2014). In theory, the relationship between chlorophyll and the three band spectrum can be expressed as:

$$\text{chlorophyll}-a = [(R_{rs}(\lambda_1)^{-1}) - (R_{rs}(\lambda_2)^{-1})]R_{rs}(\lambda_3) \quad \text{Equation (13)}$$

where λ_1 corresponds to a wavelength that is maximally sensitive to chl-*a* absorption, λ_2, is closely located to λ_1 and corresponds to a region least sensitive to chl-*a* absorption while λ_3 corresponds to a region minimally affected by absorption by chl-*a*, suspended sediments, and CDOM (Gitelson et al., 2007). Gitelson et al. (2007) suggested that λ_3 be selected in the NIR range beyond 710 nm.

In order to determine which OLI band to assign to λ_1, laboratory-derived chlorophyll-*a* values (which ranged from 6 – 147 μg l^{-1}) and R_{rs} data from 20 sampling stations in North Carolina and Rhode Island were regressed with λ_1 as band 1 (443 nm), band 2 (482 nm), and band 4 (655 nm) (Figure 6). During this exercise, OLI band 3 (centered at 562 nm) was chosen for λ_2 because the bandwidth corresponds to a chlorophyll-*a* absorbance minimum in standard laboratory spectra (Jeffrey et al., 1997) and corresponds with a depression in phytoplankton absorption curves in Thrane et al. (Figure 5A). OLI band 5 (centered at 865 nm) was chosen for λ_3 because it meets the Gitelson et al., (2007) criteria of being positioned beyond 710 nm in the NIR where water absorption is at its maximum and light absorption by CDOM, chl-*a* and NAP is zero.

Results showed that OLI band 1 (centered at 443 nm) best satisfied the Dall'Olmo et al. (2003) criteria for λ_1 selection with the resulting coefficient of determination of 0.83 (Figure 6). When λ_1 was assigned to band 2, the resulting coefficient of determination continued to be strong (R^2= 0.86; Figure 6). When λ_1 was assigned to band 4, the resulting coefficient of determination was also strong (R^2= 0.67; Figure 6). Linear regression of chlorophyll-*a* versus R_{rs} resulted in the following three-band relationships:

$$\text{chl}-a = 32.989[(R_{rs}(443)^{-1} - R_{rs}(562)^{-1})R_{rs}(865)] + 12.116 \quad \text{Equation (14)}$$

$$\text{chl}-a = 60.703[(R_{rs}(482)^{-1} - R_{rs}(562)^{-1})R_{rs}(865)] + 10.386 \quad \text{Equation (15)}$$

$$\text{chl}-a = 61.176[(R_{rs}(655)^{-1} - R_{rs}(562)^{-1})R_{rs}(865)] + 26.186 \quad \text{Equation (16)}$$

3.4.2 Blue and green band ratio combinations

Empirical blue-green (440 – 550 nm) spectral band ratios are the most common types of ocean color algorithms used for chl-*a* retrievals because most of the phytoplankton absorption occurs within this region of the visible spectrum (Blondeau-Patissier et al., 2014).

However, in optically complex waters such as inland and coastal waters, reflectance band ratios become less sensitive to changes in chlorophyll concentrations because of increasing absorption of light by CDOM (Figure 5b; Dierssen, 2010; Keith et al., 2002) and total suspended matter (Figure 5c). Linear regression of chl *a* versus OLI band 2 (BN2) to OLI band 3 (BN3) R_{rs} ratios resulted in the following relationship (Figure 6):

$$\text{chl}-a = 247.6\exp[-3.582(R_{rs}(482)/R_{rs}(562))] \quad \text{Equation (17)}$$

Linear regression of laboratory measured chl-*a* values versus Landsat-8 band 3/band 2 R_{rs} ratios resulted in the following relationship (Figure 6):

$$\text{chl}-a = 3.112\exp[1.223(R_{rs}(562)/R_{rs}(482))] \quad \text{Equation (18)}$$

3.4.3 Fluorescent Line Height (FLH) Blue and Violet reflectance models—The FLH Blue and Violet models are also band difference algorithms that were specifically formulated for Landsat-8 to quantify solar-induced fluorescence (Beck et al., 2016). FLH Blue and Violet algorithms are based on the difference in height of the green peak in the visible spectrum relative to the blue or violet minima, respectively, in spectral data (Beck et al., 2016; Figure 6A). The FLH Violet algorithm was designed to incorporate spectral data from the newly added Coastal band (Band 1; Beck et al, 2016).

Linear regression of laboratory measured chlorophyll-*a* values versus R_{rs} resulted in the following relationships (Figure 6):

FLH Blue reflectance model

$$\text{chl}-a = 6059.4(R_{rs}(562) - [(R_{rs}(655) + (R_{rs}(482) - R_{rs}(655))]) + 15.083 \quad \text{Equation (19)}$$

FLH Violet reflectance model

$$\text{chl}-a = 4705.2(R_{rs}(562) - [(R_{rs}(655) + (R_{rs}(443) - R_{rs}(655))]) + 16.578 \quad \text{Equation (20)}$$

Model validation was conducted using measured chl-*a* values from 15 stations in Jordan Lake and the Rhode Island ponds and model predicted values (Table 4).

Results showed that the best performing algorithms were the three-band algorithms with λ_1 centered at 443 nm ($R^2 = 0.66$) and 482 nm ($R^2 = 0.58$) (Table 5; Figure 7). The FLH violet and blue reflectance algorithms had similar R-squared values ($R^2 = 0.52$ and $R^2 = 0.51$, respectively; Figure 7). The blue and green ratio combinations were poor performers ($R^2 = 0.18$) for both ratio combinations (Figure 7). Results from the three-band algorithm with λ_1 centered at 655 nm were not graphically presented due to its very poor performance ($R^2 =$

0.05, RMSE = 19.8 μg l^{-1}, MAPE = 102 %). A comparison of all algorithms for the best predictive ability (Table 5; Figure 7) showed that the three-band algorithm with λ_1 centered at 443 nm had the lowest RMSE (8.9 μg l^{-1}), MAPE (33.5%) and MAE (7.0 μg l^{-1}) (Table 5).

Scatterplots of the differences between observed and predicted chl-*a* values showed that the residuals were randomly distributed, indicating that the linear models provided a decent fit to the data (Figure 8).

3.4.4 Evaluation of SWIR atmospheric correction on the estimation of chl-a values—Using Jordan Lake images from Autumn 2014 (October 25), Winter 2015 (28 January 2015), Spring 2015 (2 April 2015) and Summer 2015 (7 July 2015), comparisons were made between chl-*a* predicted from Equation 13, R_{rs} corrected for Rayleigh effects only, and R_{rs} corrected for both Rayleigh and aerosol effects. Results showed that for the four example images used in this comparison, predicted chl-*a* concentrations were higher (overestimated) by an overall average of approximately 19% for those pixels not corrected for aerosols. For each image, the range varied from approximately 13 - 32 % (Table 6).

4. Spatial and Temporal Maps of Chlorophyll *a* and Trophic State of Jordan Lake and Newport Water Supply Reservoirs

As a demonstration of the potential of the OLI to forecast algal bloom distribution as well as trophic state (Carlson, 1977) for drinking water reservoirs at a variety of spatial scales, we derived chl-*a* concentrations for Jordan Lake and the Newport Water Supply using the validated three-band algorithm (Equation 13). Using the NASA SeaDAS program to extract pixels from Landsat-8 imagery, the magnitude of algal blooms and their location are mapped for each water body from five Landsat-8 images from 2014 and 2015 (Figures 8 and 9).

Figure 9 shows an example of the spatial and temporal distribution of chl-*a* in Jordan Lake for three L-8 images representing Autumn 2014 (image date - October 24, 2014), Winter 2015 (image date - January 28, 2015), and Spring 2015 (image date - April 2, 2015). During Autumn 2014, Jordan Lake and adjoining feeder streams and creeks ranged from mesotrophic (chl-*a* less than 20 μg l^{-1}; Carlson, 1977) to eutrophic (chl-*a* ranging from 20 - 56 μg l^{-1}; Carlson, 1977) conditions along the main stem of Jordan Lake and Haw River. In contrast, the northern reach was characterized as highly eutrophic (chl-*a* greater than 56 μg l^{-1}; Carlson, 1977). During Winter 2015, the entire Jordan Lake system was characterized as predominantly mesotrophic (Figure 9). In Spring 2015, Jordan Lake was characterized as predominantly eutrophic (Figure 9).

For the Newport Water Supply reservoirs, Landsat image LC80120312015224LGN00_sr on August 12, 2015 (Figure 10) acquired concurrently with field sampling showed the nine reservoirs generally ranged from mesotrophic to eutrophic conditions. Hypereutrophic areas of intense algal blooms were embedded in northwest-southeast trending bands of elevated chlorophyll-*a* in Watson Reservoir and in Nonquit Pond (Figure 10). Generally, these reservoirs were characterized by mesotrophic to eutrophic conditions with floating macroalgae (as suggested by a spectral peak at 865 nm). In comparison, the seven remaining

ponds were characterized as generally mesotrophic to eutrophic reservoirs with low to moderate chl-*a* levels.

5. Conclusions

The most promising approach for routinely monitoring algal blooms and HABs in lakes, ponds, and reservoir systems is to use sensors with high spatial resolutions and low signal-to-noise ratios on space-based platforms. By linking these systems with simple reflectance algorithms, concentrations of chl-*a* derived from spectral data can be used to maximize temporal and spatial coverage of inland lakes, coastal freshwater ponds and estuaries for algal bloom detection. Forecasts of changes in biomass concentration or phytoplankton bloom location within a lake or reservoir can then be used as an early warning indicator to identify potential areas (such as water system intakes) for additional field-based investigations (Augusto-Silva et al., 2014).

In this study, we used spectral data from the Landsat-8 OLI sensor and a 3 band reflectance model to map algal blooms in a large recreational and drinking water reservoir and several smaller drinking water reservoirs which ranged in size from tens of thousands to hundreds of acres. This capability provides water managers with a new tool to assess the condition of their water bodies more frequently and synoptically which allows them to focus limited resources on risk mitigation of potential harmful blooms. Using Landsat-8 LSR 30 m data acquired from drinking water reservoirs in North Carolina and Rhode Island, we evaluated several established satellite reflectance algorithms for estimating chl-*a* concentrations as potential resources to monitor changes in water quality. Through this evaluation process, a simple approach and 3 band spectral algorithm was validated that uses the OLI sensor violet, green and NIR spectral bands to accurately predict chl-*a* concentrations in drinking water reservoirs of various areal extents. We applied the algorithm to several atmospherically and sun-glint corrected Landsat-8 LSR images to map the spatial and temporal distribution as well as the seasonal variability of chlorophyll in the Jordan Lake reservoir.

We showed, in a single day image of the reservoirs of the Newport Water Supply, that a synoptic image can provide valuable information on the magnitude of localized high phytoplankton concentrations that may be the short-term environmental response to point source and non-point source nutrient loading.

Acknowledgments

We thank K. DeVilbiss (NCDEQ DWR); M. Hale (NCDEQ DWR); J. Smith (NCDEQ DWR); E. Morris (NCDEQ DWR); and D. Owen (NCDEQ DWR) for Jordan Lake sampling. We also thank R. Lunetta (USEPA), B. Schaeffer (USEPA), W. Salls (ORISE Fellow), A. Kuhn-Hines (USEPA) and J. LiVolsi (USEPA) for their insightful and valuable review comments.

Funding

This work was supported by the NASA Ocean Biology and Biogeochemistry Program/Applied Sciences Program under proposal 14-SMDUNSOL14-0001 and by EPA, NOAA, and USGS Toxic Substances Hydrology Program. This work was also supported by the U.S. Environmental Protection Agency Office of Research and Development and the Safe and Sustainable Waters Resources Program.

References

Arar, EJ., Collins, GB. Method 445.0-In Vitro Determination of Chlorophyll-a and Pheophytin-a in Marine and Freshwater Algae by Fluorescence. US Environmental Protection Agency; Washington, DC: 1997.

Augusto-Silva PB, Ogasashawa I, Barbosa CC, Carvelho LAS, Jorge DSF, Fornari CI, Stech JL. Analysis of MERIS reflectance algorithms for estimating chlorophyll–*a* concentration in a Brazillian Reservoir. Remote Sensing. 2014; 6:11689–117077.

Beck R, Zhan S, Liu H, Tong S, Yang B, Xu M, Ye Z, et al. Comparison of satellite reflectance algorithms for estimating chlorophyll-*a* in a temperate reservoir using coincident hyperspectral aircraft imagery and dense coincident surface observations. Remote Sensing of Environment. 2016; 178:15–30. http://dx.doi.org/10.1016/j.rse.2016.03.002.

Blondeau-Patissier D, Gower JFR, Dekker AG, Phinn SR, Brando V. A review of ocean color remote sensing methods and statistical techniques for the detection, mapping and analysis of phytoplankton blooms in coastal and open oceans. Progress in Oceanography. 2014; 123:123–144.

Carlson RE. A trophic state index for lakes. Limnology and Oceanography. 1977; 22(2):361–369.

Concha, JA., Schott, JR. Retrievel of color producing agents in Case 2 waters using Landsat 8. Remote Sensing of Environment. 2016. (in press)http://dx.doi.org/10.1016/j.rse.2016.03.0318

Cox C, Munk W. Statistics of the Sea Surface Derived from Sun Glitter. Journal of Marine Research. 1954; 13:198–227.

Dall'Olmo G, Gitelson AA, Rundquist DC. Towards a unified approach for remote estimation of chlorophyll-a in both terrestrial and vegetation and turbid productive waters. Geophysical Research Letters. 2003; 30:1038. http://dx.doi.org/10.1029/2003GL018065.

Dekker, AG., Hestir, EL. Evaluating the feasibility of systematic inland water quality monitoring with satellite remote sensing. Canberrra, Australia: Commonwealth Scientific and Industrial Research Organization; 2012. p. 123

Dierssen HM. Perspectives on empirical approaches for ocean color remote sensing of chlorophyll in a changing climate. Proceeding of the National Academy of Sciences of the United States of America. 2010; 107:170073–17078.

Emberton S, Chittka L, Cavallaro A, Wang M. Sensor Capability and Atmospheric Correction in Ocean Colour Remote Sensing. Remote Sensing. 2016; 8:1–31.

Franz BA, Bailey SW, Kuring N, Werdell PJ. Ocean color measurements with the Operational Land Imager on Landsat-8: implementation and evaluation in SeaDAS. Applied Remote Sensing. 2015; 2:096070-1–096060-6. DOI: 10.1117/I.JRS.9.096070

Garaba SP, Zielinski O. Comparison of remote sensing reflectance from above-water and in-water measurements west of Greenland, Labrador Sea, Denmark Strait, and west of Iceland. Optics Express. 2013; 21(13):15938–50. DOI: 10.1364/OE.21.015938 [PubMed: 23842380]

Gerace AD, Schott JR. Over-water atmospheric correction for Landsat's new OLI sensor. Proceedings of SPIE. 2012; 8372:837211. http://dx.doi.org/10.1117/12.919304.

Gitelson AA, Gurlin D, Moses WJ, Barrow T. A bio-optical algorithm for the remote estimation of the chlorophyll-*a* concentration in case 2 waters. Environmental Research Letters. 2009; (4)

Gitelson AA, Schalles JF, Hladik CM. Remote chlorophyll-*a* retrieval in turbid, productive estuaries: Chesapeake Bay case study. Remote Sensing of Environment. 2007; 109:464–472. DOI: 10.1016/j.rse.2007.01.016

Graham JL. Harmful Algae Blooms. US Geological Survey Fact Sheet. 2006:2006–3147.

Gordon HR, Wang M. Retrieval of water-leaving radiance and aerosol optical thickness over the oceans with SeaWiFS: a preliminary algorithm. Applied Optics. 1994; 33(3):443–452. [PubMed: 20862036]

Hedley JD, Harborne AR, Mumby PJ. Simple and robust removal of sun glint for mapping shallow-water benthos. International Journal of Remote Sensing. 2005; 26(10):2107–2112. DOI: 10.180/01431160500034086

Hochberg EJ, Andrefouet S, Tyler MR. Sea surface correction of high spatial resolution Ikonos images to improve bottom mapping in near-shore environments. IEEE Transactions on Geoscience and Remote Sensing. 2003; 41:1724–1729.

Hooker SB, Lazin G, Zibordi G, McLean S. An evaluation of above-and In-water methods for determining water-leaving radiance. Journal of Atmospheric and Oceanic Technology. 2002; 19:486–514.

Hu C. A novel ocean color index to detect floating algae in the global oceans. Remote Sensing of Environment. 2009; 113:2118–2129. DOI: 10.1016/j.re.2009.05.012.

Hu C, Chen Z, Clayton TD, Swarzenski P, Brock JC, Muller-Karger FE. Assessment of estuarine water-quality indicators using MODIS medium-resolution bands: initial results from Tampa Bay, FL. Remote Sensing of Environment. 2004; 93:423–441.

Jeffrey, SW., Mantoura, RFC., Bjornland, T. Part IV. Data for the identification of 47 key phytoplankton pigments. In: Jeffrey, SW.Mantoura, RFC., Wright, SW., editors. Phytoplankton pigments in oceanography: guidelines to modern methods. UNESCO Publishing; 1997. p. 661

Keith DJ, Schaeffer BA, Lunetta RS, Gould RW Jr, Rocha K, Cobb DJ. Remote sensing of selected water-quality indicators with the hyperspectral imager for the coastal ocean (HICO) sensor. International Journal of Remote Sensing. 2014; 35(9):2927–2962. http://dx.doi.org/10.1080/01431161.2014.894663.

Keith, DJ. Chapter 7. Estimating Chlorophyll Conditions in Southern New England Coastal Waters from Hyperspectral Aircraft Remote Sensing. In: Wang, Yeqiao, editor. Remote Sensing of Coastal Environments. CRC Press; 2010.

Keith DJ, Yoder JA, Freeman SA. Spatial and Temporal Distribution of Coloured Dissolved Organic Matter (CDOM) in Narragansett Bay, Rhode Island: Implications for phytoplankton on Coastal Waters. Estuarine, Coastal and Shelf Science. 2002; 55:705–717. DOI: 10.1006/ecss.2001.0922

Klemas V. Remote sensing of algal blooms: an overview with case studies. Journal of Coastal Research. 2012; 28:34–43.

Knaeps E, Dogliotti AI, Raymaekers D, Ruddick K, Sterckx S. *In situ* evidence of non-zero reflectance in the OLCI 1020 nm band for a turbid estuary. Remote Sensing of Environment. 2012; 120:113–144.

Kou L, Labrie D, Chylek P. Refractive indices of water and ice in the 0.65-2.5 –μm spectral range. Applied Optics. 1993; 32:3531–3540. [PubMed: 20829977]

Kudela RM. Application of hyperspectral remote sensing to cyanobacterial blooms in inland waters. Remote Sensing of Environment. 2015; 167:196–205.

Lee DS, Storey JC, Choate MJ, Hayes R. Four years of landsat-7 on-orbit geometric calibration and performance. IEEE Transactions on Geoscience and Remote Sensing. 2004; 42:2786–2795.

Lemasson C, de Marsac N Tandeau, Cohen-Bazire G. Role of Allophycocyanin as a Light-Harvesting Pigment in Cyamobacteria. Proc Nat Acad Sci USA. 1973 Nov; 70(11):3130–3133. [PubMed: 16592117]

Li Y. Atmospheric correction of SeaWiFS imagery for turbid coastal and inland waters: comment. Applied Optics. 2003; 42:893–895. [PubMed: 12617203]

Mayo M, Gitelson A, Yacobi YZ, Ben-Avraham Z. Chlorophyll distribution in Lake Kinneret determined from Landsat Thematic Mapper data. Remote Sensing. 1995; 106(1):175–182.

Mishra S, Mishra DR. Normalized difference chlorophyll index: A novel model for remote estimation of chlorophyll *a* concentration in turbid productive waters. Remote Sensing of Environment. 2012; 117:394–406.

Mobley CD. Polarized reflectance and transmittance properties of windblown sea surfaces. Applied Optics. 2015; 54(15):4828–4849. [PubMed: 26192522]

Moses WJ, Gitelson AA, Berdnikov S, Povazhnyy V. Estimation of chlorophyll-a concentration in case II waters using MODIS and MERIS data-successes and challenges. Environmental Research Letters. 2009; 4:045005.

Mustard JF, Staid MI, Fripp WJ. A semianalytical approach to the calibration of AVIRIS data to reflectance over water application in a temperate estuary. Remote Sensing of Environment. 2002; 75:335–349.

NC DENR. Ambient Lakes Monitoring Program (ALMS) Quality Assurance Project Plan. NC Department of Environment and Natural Resources, Division of Water Resources, Environmental Sciences Section, Intensive Survey Branch. 2014:53. EPA Approved March 28, 2014, Version 2.0.

NCDENR. B. Everett Jordan Reservoir, North Carolina Phase I Total Maximum Daily Load. Raleigh. 2007

Ohio EPA. Public Water System Harmful Algal Bloom, Response Strategy. Ohio Environmental Protection Agency, Division of Drinking and Ground Waters; 2013. p. 82

Pope RM, Fry ES. Absorption spectrum (380-700 nm) of pure water. II. Integrating cavity measurements. Applied Optics. 1997; 36:8710–8723. [PubMed: 18264420]

Poryvkina, L., Babichenoko, S., Leeben, A. Analysis of Phytoplankton Pigments by Excitation Spectra of Fluorescence. Proceedings of EARSeL-SIG-Workshop LIDAR; Dresden/FRG. June 16-17; 2000. p. 224-232.

Rabinowitch, E., Govindjee. Photosynthesis. John Wiley and Sons; New York: 1969. Chapter 9 The Photosynthetic Pigments; p. 102-123.

Reif M. Remote sensing for inland water quality monitoring: A US Army Corps of Engineers Perspective. 2011:44.Engineer Research and Development Center/Environmental Laboratory Technical Report (ERDC/EL TR -11-13)

Rhode Island Department of Environmental Management (RIDEM). Draft 2015 Sample Plan for RIDEM Water Quality Monitoring in the Newport Reservoirs. 2015:59.

Ruddick KG, Ovidio F, Rijkeboer M. Atmospheric correction of SeaWiFS imagery for turbid coastal and inland waters. Applied Optics. 2000; 39:897–912. [PubMed: 18337965]

Schalles JF, Gitelson A, Yacobi YZ, Kroenke AE. Chlorophyll estimations using whole seasonal, remotely sensed high spectral resolution data for a eutrophic lake. Journal of Phycology. 1998; 34:383–390.

Shanmugan P. An atmospheric correction algorithm for the remote sensing of complex waters. Ann Geophys. 30:2012–220. 203–220.

Shi W, Wang M. An assessment of the black pixel assumption for MODIS SWIR bands. Remote Sensing of Environment. 2009a; 113:1587–1597. DOI: 10.1016/j.rse.2007.02.013.

Siegel DA, Wang S, Maritorena S, Robinson W. Atmospheric correction of satellite ocean color imagery: The black pixel assumption. Applied Optics. 2000; 39:3582–3591. [PubMed: 18349929]

Storey, Lee JK, Choate M. Geometeric performance comparisons between the OLI and the ETM+ Proceedings of the PECORA Conference. 2008

Stumpf, RP., Arnone, RA., Gould, RW., Martinolich, PM., Ransibrahmanakul, V. A partially coupled ocean-atmosphere model for retrieval of water-leaving radiance from SeaWiFS in coastal waters. In: Hooker, SB., Firestone, ER., editors. NASA Tech Memo. Vol. 22. NASA, Goddard Space Flight Center; Greenbelt, Maryland: 2003. p. 51-59.2003-206892, SeaWiFS Postlaunch Technical Report Series2003

Thrane JE, Hessen DO, Anderson T. The Absorption of Light in Lakes: Negative Impact of Dissolved Organic Carbon on Primary Productivity. Ecosystems. 2014; 17:1040–1052. DOI: 10.1007/s10021-014-9776-2

Town of Portsmouth, Rhode Island. Comprehensive Community Plan. 2002 Jul.:323.

Turner D. Remote sensing of chlorophyll-*a* concentrations to support the Deschutes Basin Lake and reservoir TMDLs. Report to the US Environmental Protection Agency for 104b3 2009 grant, component. 2010; 4:1–43.

United States Environmental Protection Agency. National Water Quality Inventory: Report to Congress - 2004 Reporting Cycle. 2009 Jan.EPA 841-R-08-001

United States Geological Survey. Provisional Landsat 8 Surface Reflectance Product Guide: Earth Explorer Version. Version 2.2. Department of the Interior. 2016 Jul.

Vanhellemont, Q., Ruddick, K. Paper submitted for the proceedings of the 2016 ESA Living Planet Symposium ESA Special Publication SP-740. Prague, Czech Republic: 2016. May 9-13. ACOLITE for Sentinel-2: Aquatic Applications of MSI Imagery. 2016

Vanhellemont Q, Ruddick K. Advantages of high quality SWIR bands for ocean color processing: Examples from Landsat-8. Remote Sensing of Environment. 2015; 161:89–106. http://dx.doi.org/10.1016/j.rse.2015.02.007.

Vanhellemont Q, Ruddick K. Turbid wakes associated with offshore wind turbines observed with Landsat 8. Remote Sensing of Environment. 2014a; 145:105–115.

Vertucci FA, Likens GF. Spectral reflectance and water quality of Adirondack mountain region lakes. Limnol Oceanogr. 1989; 34(8):1656–1672.

Vos WL, Donze M, Bueteveld H. On the reflectance spectrum of algae in water: The nature of the peak at 700 nm and its shift with varying concentrations. Communication of Sanitary Engineering and Water Management, Delft, The Netherlands. 1986Technical Report 86-22

Wang M, Shi W, Tang J. Water property monitoring and assessment for China's inland Lake Taihu from MODIS-Aqua measurements. Remote Sensing of Environment. 2011; 115:841–854. http://dx.doi.org/10.1016/j.rse.2010.11.012.

Wang M. Remote sensing of the ocean contributions from ultraviolet to near-infrared using the shortwave infrared bands: simulations. Applied Optics. 2007; 46:1535–1547. [PubMed: 17334446]

Wang M, Tang J, Shi W. MODIS-derived ocean color products along the China east coastal region. Geophysical Research Letters. 2007; 34:L06611. http://dx.doi.org/10.1029/2006GL028599.

Wang M, Shi W. Estimation of ocean contribution at the MODIS near-infrared wavelengths along the east coast of the U.S.: two case studies. Geophysical Research Letters. 2005; 32:L13606. http://dx.doi.org/10.1029/2005GL022917.

Wang M, Bailey S. Correction of the Sun glint contamination on the SeaWiFS ocean and atmosphere products. Applied Optics. 2001; 40:4790–4798. [PubMed: 18360519]

World Health Organization. Guidelines for Safe Recreational Water Environments. Coastal and fresh waters. 2003; 1

Wicaksono P. The Effect of Sunglint on Satellite-Based Benthic Habitat Identification. International Journal of Advanced Research in Computer and Communication Engineering. 2012; 1(6):364–370.

Wynne TT, Stumpf R, Tomlinson MC, Dyble J. Characterizing a cyanobacterial bloom in western Lake Erie using satellite imagery and meteorological data. Limnology and Oceanography. 2012; 55:2015–2036.

Xing Q, Hu C. Mapping macroalgal blooms in the Yellow Sea and East China Sea using HJ-1 and Landsat data: Application of a virtual baseline reflectance height technique. Remote Sensing of Environment. 2016; 178:113–126. http://sx.doi.org/10.1016/j.rse.2016.02.065.

Zhang H, Wang M. Evaluation of sun glint models using MODIS measurements. J Quant Spectrosc Radiat Transf. 2010; 111:492–506.

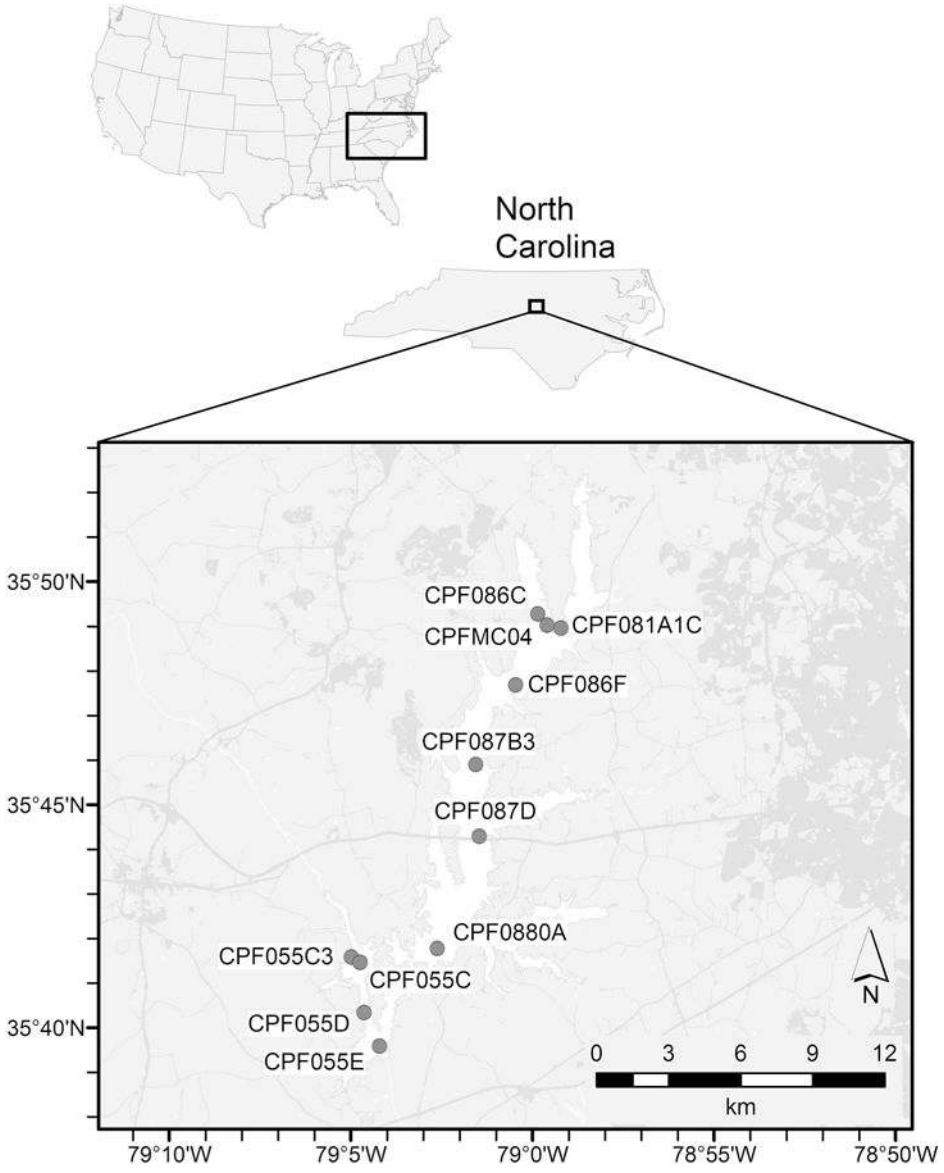

Figure 1.
NCDENR Jordan lake monitoring stations used in this study.

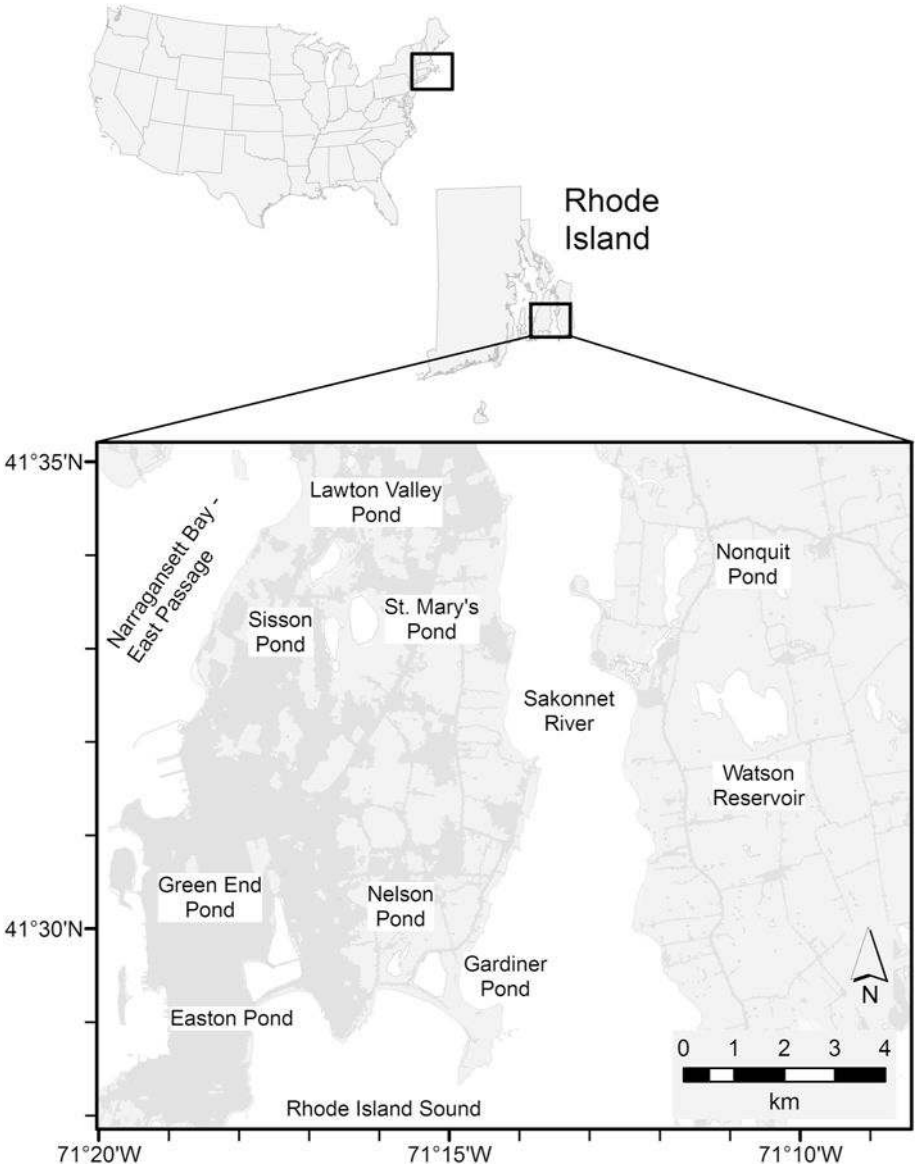

Figure 2.

Map of ponds and reservoirs that serve as drinking water sources for the Newport Water Supply (RIDEM, 2015).

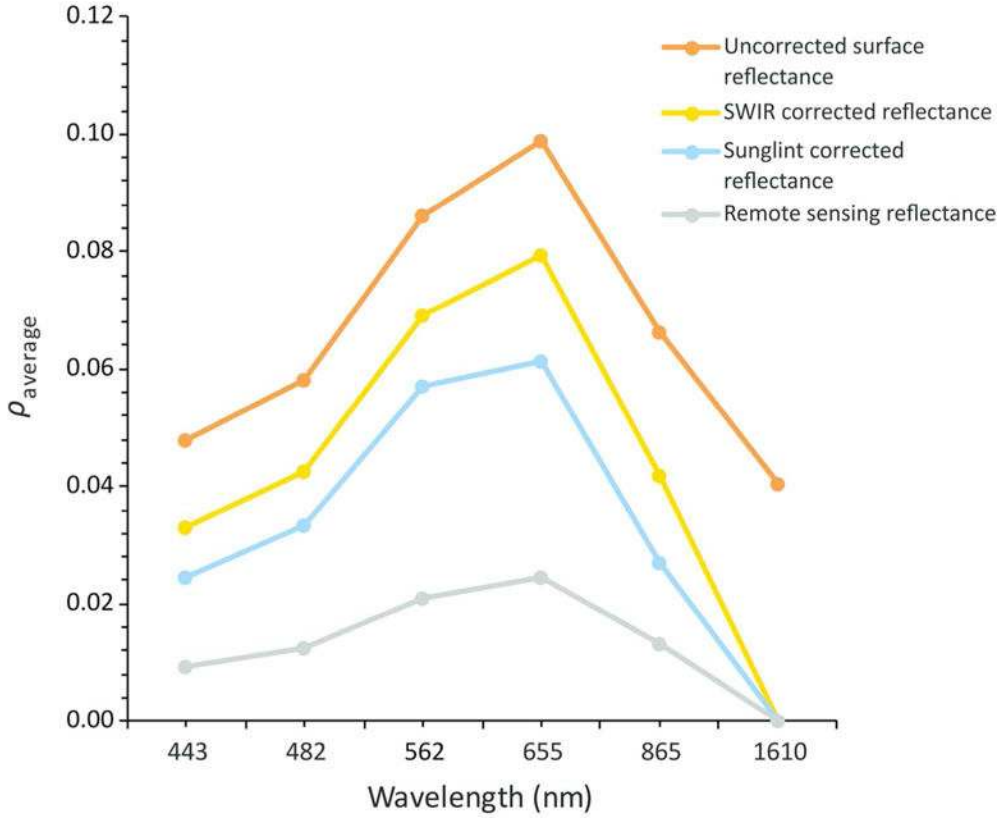

Figure 3.

An example of the retrieval of the remote sensing reflectance from the LSR data using OLI SWIR1 (center bandwidth = 1610 nm) for atmospheric correction and NIR (center bandwidth = 865 nm) for sun-glint removal on Landsat-8 image LC80160352014137LGN00_sr from Jordan Lake on May 17, 2014.

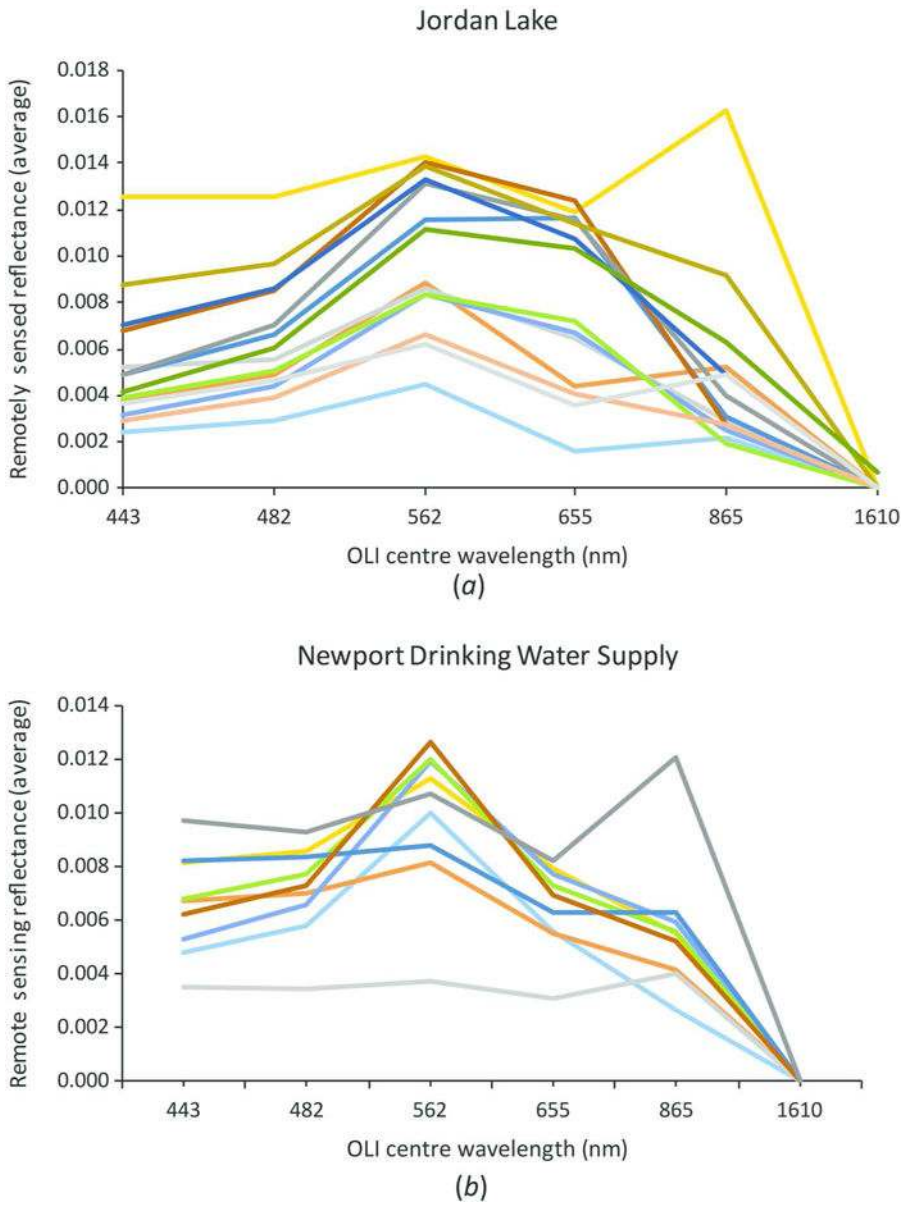

Figure 4.

a) Summary of all remote sensing reflectances (R_{rs}) retrieved from 14 L-8 images of Jordan Lake, North Carolina collected during August 2014 to July 2015. *b)* Summary of R_{rs} retrieved from L-8 image LC80120312015224LGN00_sr on August 12, 2015 from Newport, Rhode Island drinking water ponds.

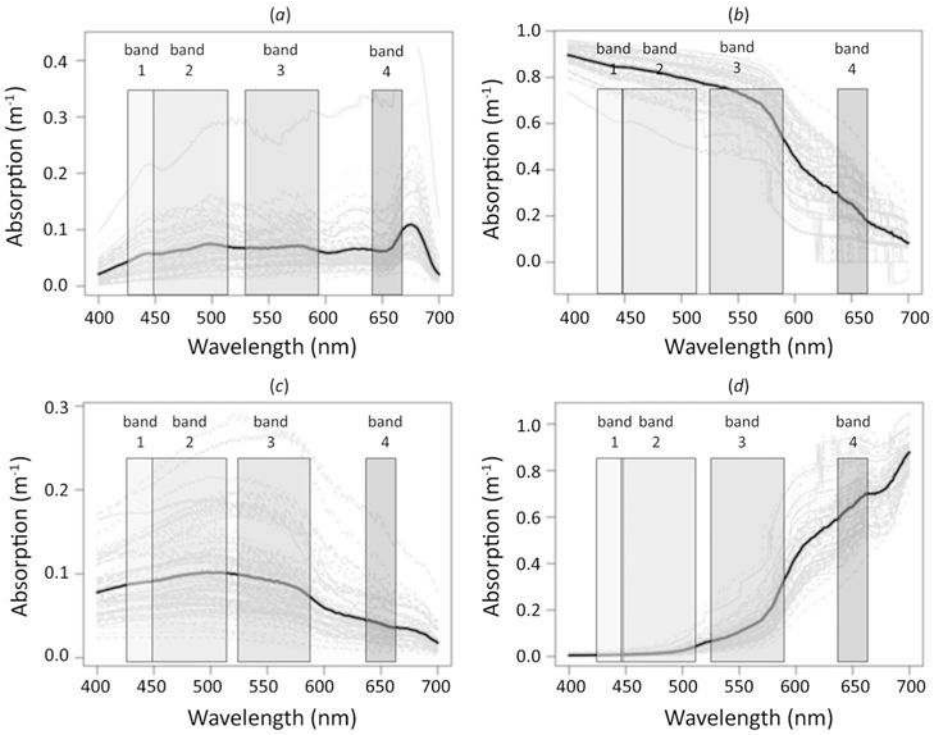

Figure 5.

Locations of Landsat 8 OLI spectral bands (BN) 1 - 4 in relation to light absorption by *(a)* phytoplankton, *(b)* coloured dissolved organic matter (CDOM), *(c)* non-algal particles (NAP), and *(d)* water from optical data from 75 boreal lakes in Northern Europe. The solid black lines represent the average of all lakes. The gray lines represent individual lakes. (Figure modified with permission from Thrane et al., 2014).

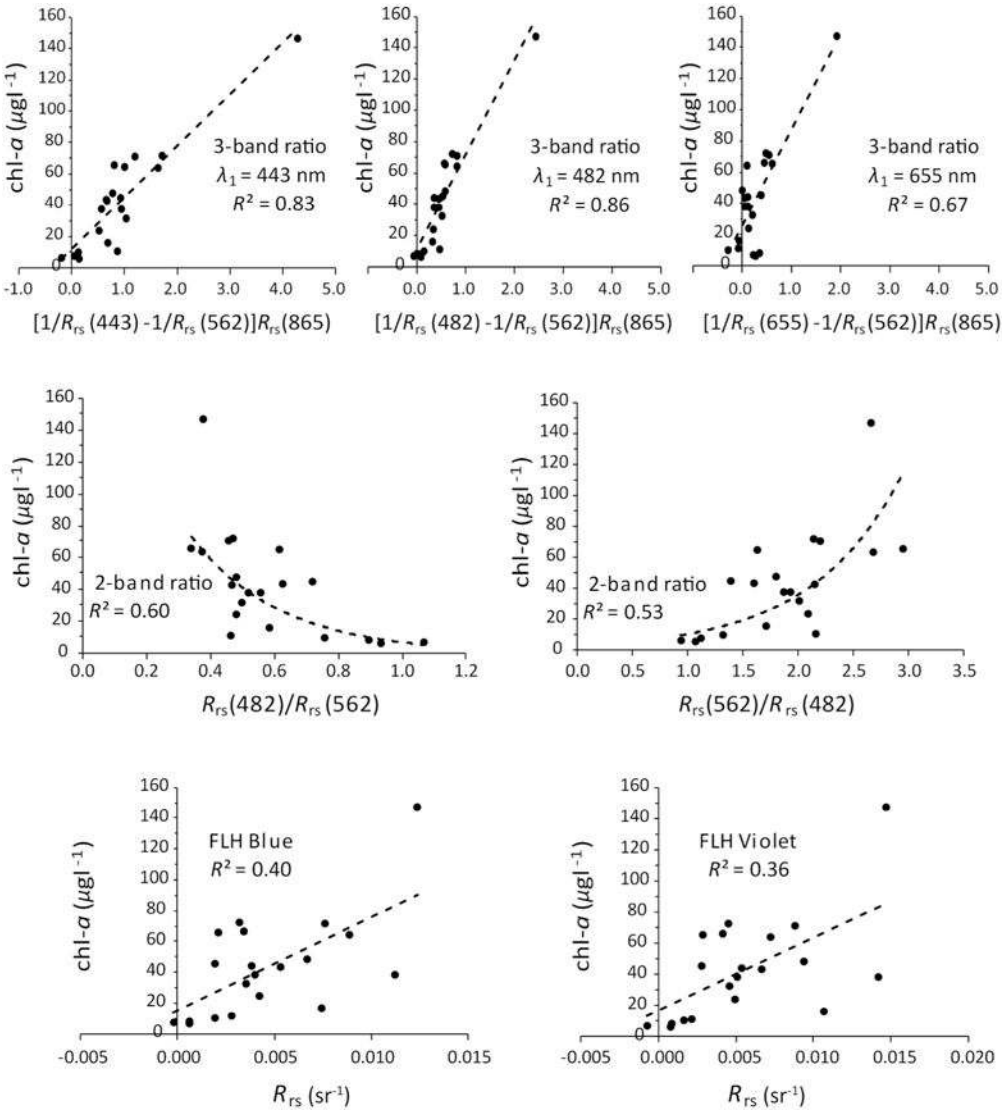

Figure 6.

Scatterplots from the linear regression of measured chl-*a* values from Jordan Lake and Newport ponds against remote sensing reflectances at 443 nm ($R_{rs}(443)$); 482 nm ($R_{rs}(482)$); 562 nm ($R_{rs}(562)$); and 865 nm ((R_{rs})865)) used in algorithm development.

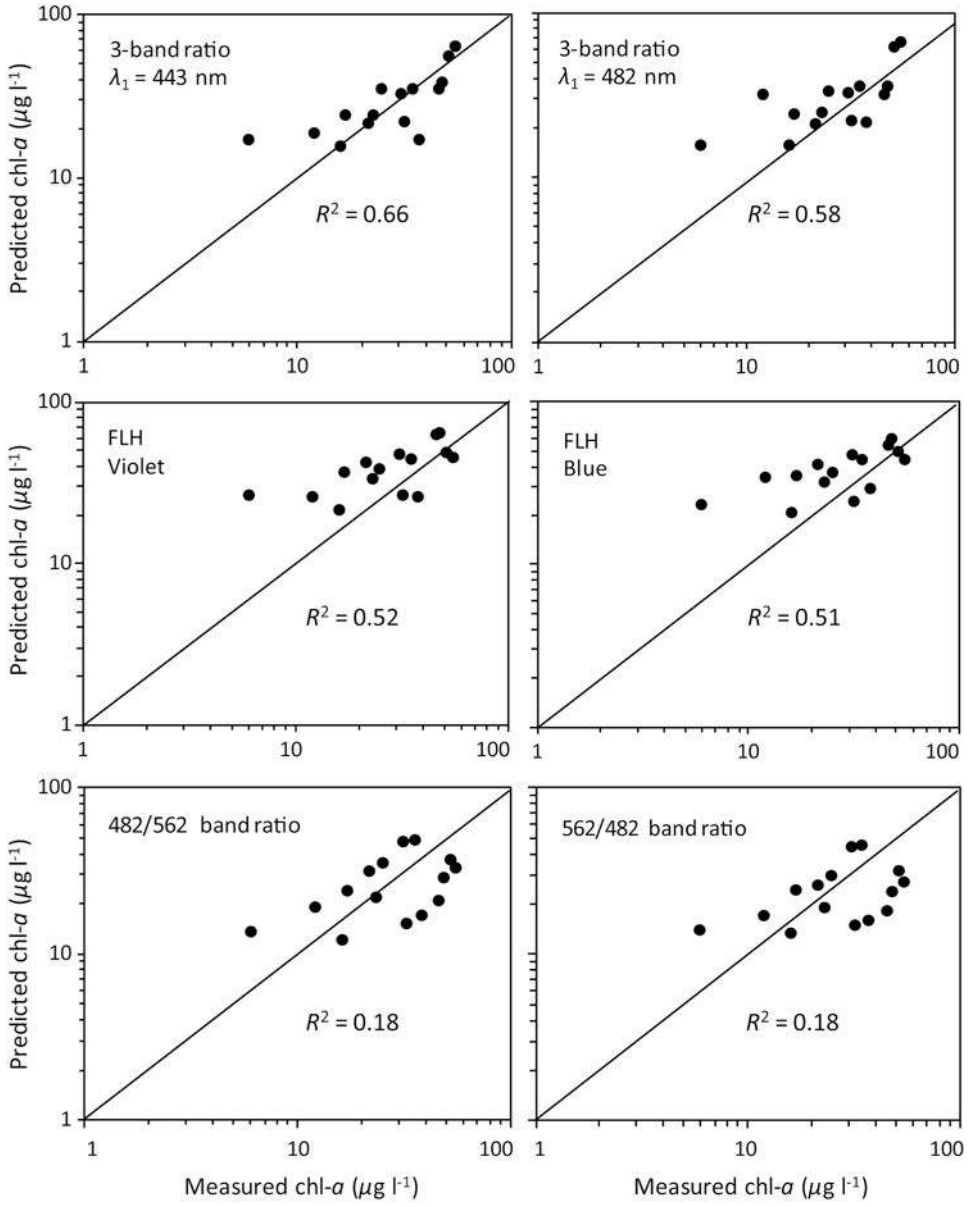

Figure 7.

Log-log scatterplots of predicted chl-*a* concentrations derived from spectral algorithms and laboratory extracted chlorophyll values from Jordan Lake and Newport Water supply reservoirs. Results from Equation 16 are not shown due to its very poor performance.

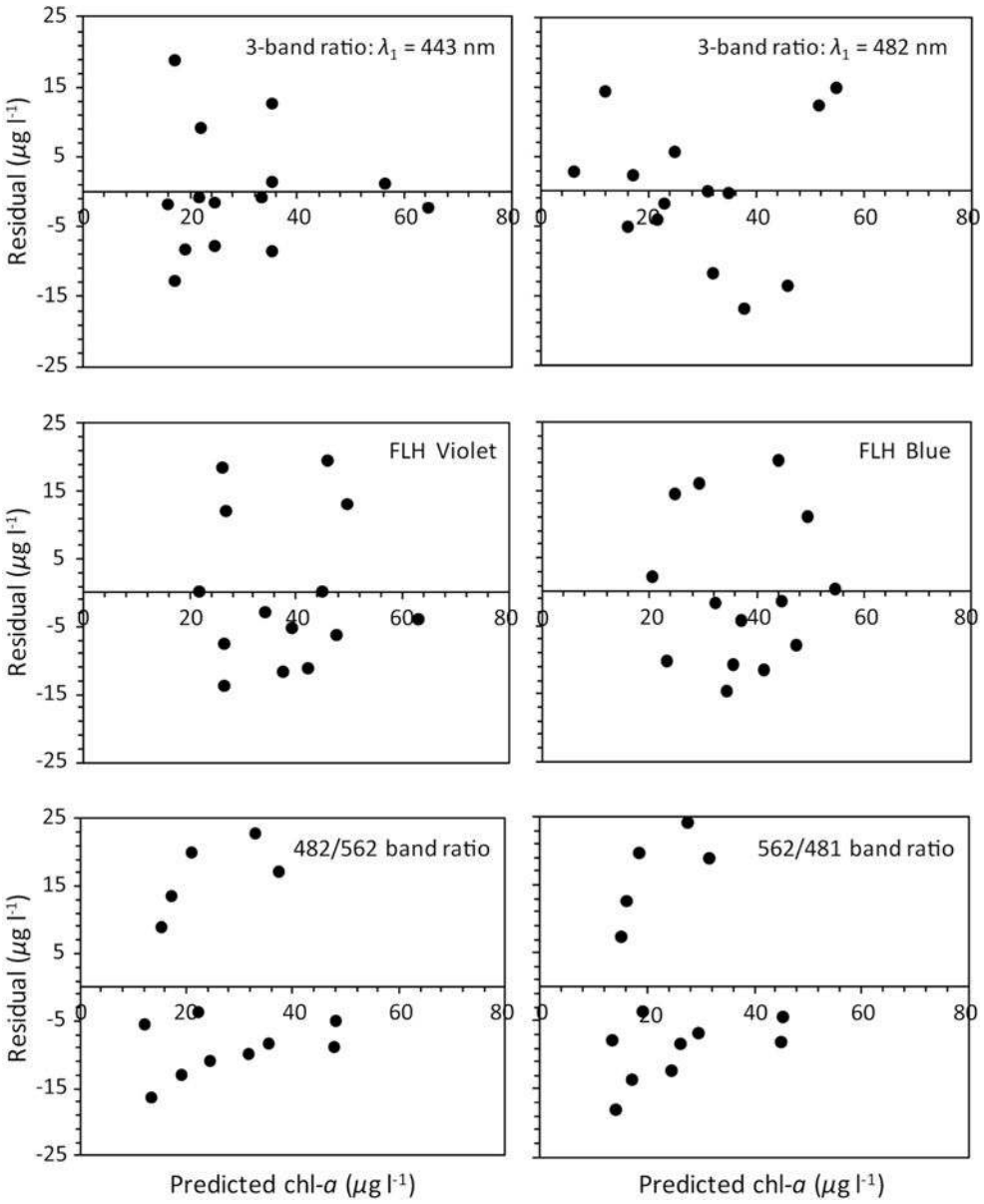

Figure 8.
Scatterplots of residual versus chl-*a* predicted from the spectral algorithms.

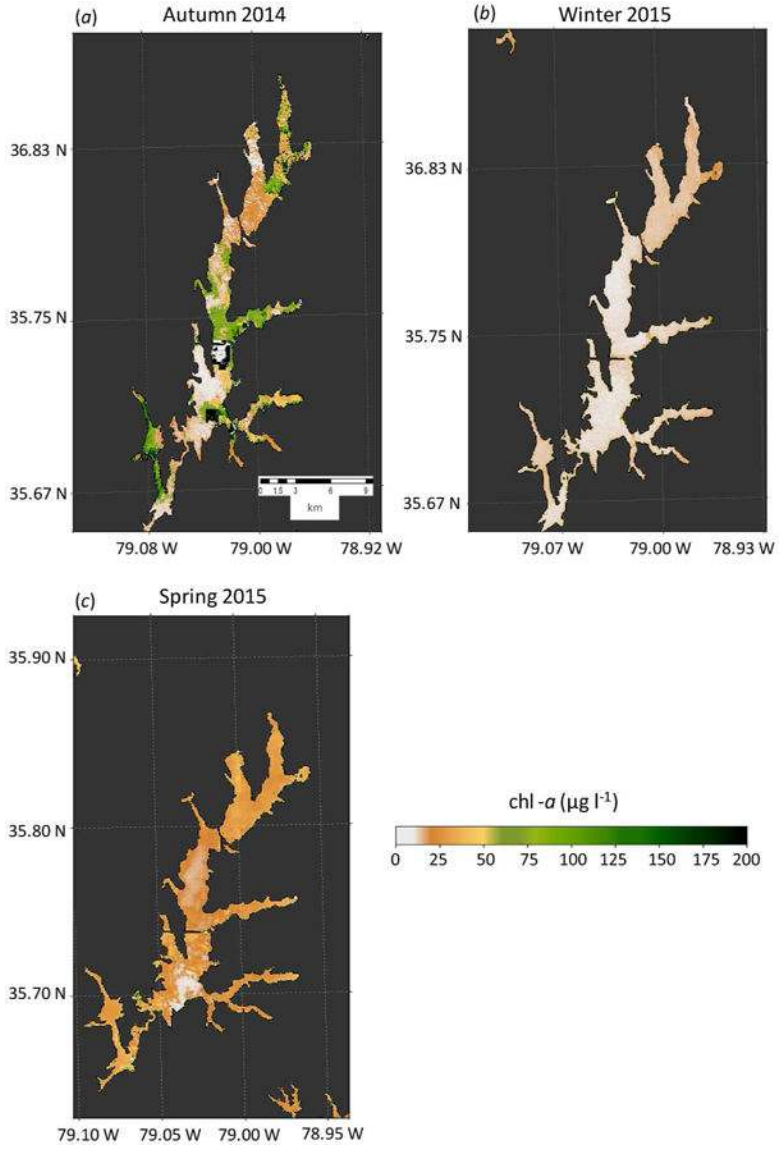

Figure 9.

Chlorophyll-*a* distribution in Jordan Lake during Autumn 2014 (L-8 image: LC80160352014265LGN00_sr), Winter 2015 (L-8 image: LC80160352015044LGN00_sr), and Spring 2015 (L-8 image: LC80160352015092LGN00_sr).

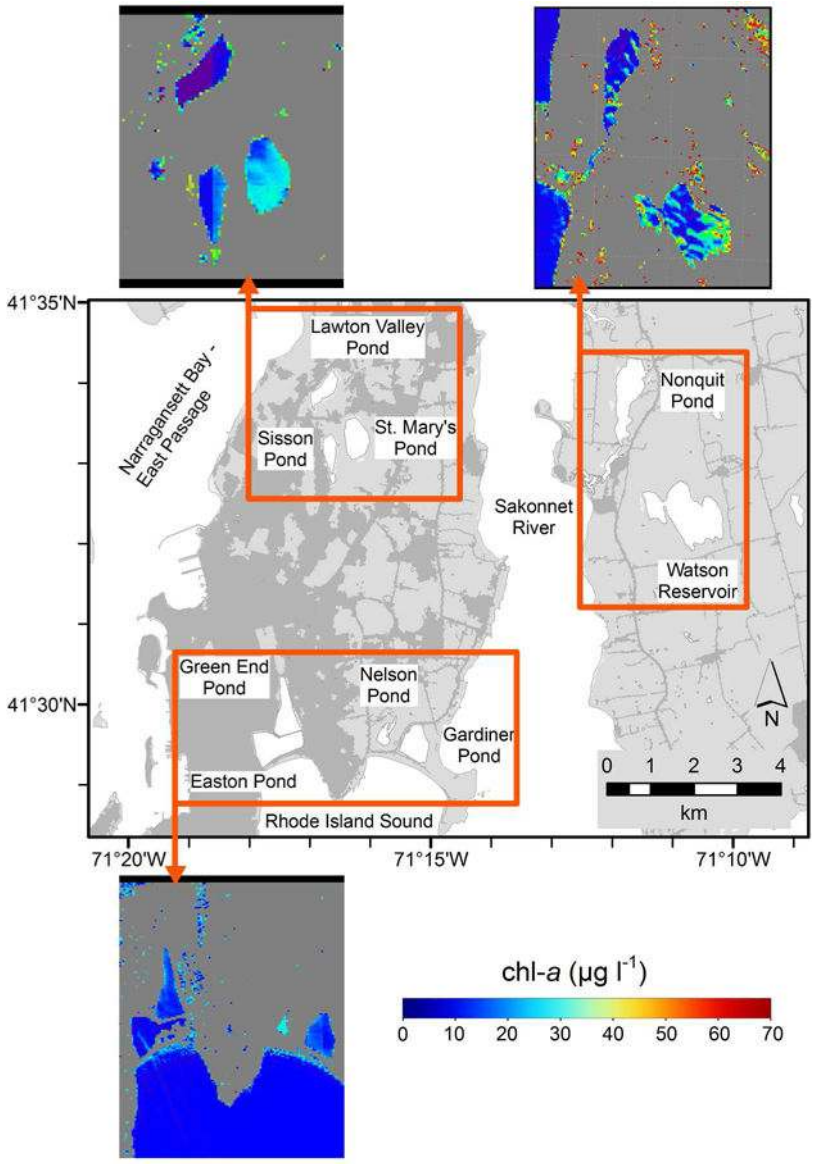

Figure 10.

Chlorophyll-*a* distribution for Newport Water Supply ponds and reservoirs on August 12, 2015 from Landsat Image LC80120312015224LGN00_sr.

Table 1

Landsat-8 images used for algorithm development.

Landsat-8 image	Path/Row	Location	Image Date
LC80160352013134LGN03_sr	16/35	North Carolina	14 May 2013
LC80160352014137LGN00_sr	16/35	North Carolina	17 May 2014
LC80160352014169LGN00_sr	16/35	North Carolina	18 June 2014
LC80160352014217LGN00_sr	16/35	North Carolina	5 August 2014
LC80160352014233LGN00_sr	16/35	North Carolina	21 August 2014
LC80160352014249LGN00_sr	16/35	North Carolina	6 September 2014
LC80120312015128LGN00_sr	12/31	Rhode Island	10 May 2015
LC80120312015176LGN00_sr	12/31	Rhode Island	25 June 2015
LC80120312015192LGN00_sr	12/31	Rhode Island	11 July 2015
LC80120312015224LGN00_sr	12/31	Rhode Island	12 August 2015
LC80120312015240LGN00_sr	12/31	Rhode Island	28 August 2015

Table 2

Landsat-8 OLI spectral bands used in this study band averaged, Rayleigh reflectance (τ), and ratio of longest to shortest wave bands (σ_i) used for each waveband.

Band	Bandwidth range (μm)	Center bandwidth (μm)	Pixel resolution (m)	τ	σ_i
1	0.430 - 0.450	0.443	30	0.235	1.000
2	0.450 - 0.510	0.482	30	0.168	0.967
3	0.530 - 0.590	0.562	30	0.090	0.898
4	0.640 - 0.670	0.655	30	0.048	0.818
5	0.850 – 0.880	0.865	30	0.015	0.638
6	1.570 – 1.650	1.610	30	0.001	0.000

Table 3

NCDENR and RIDEM stations, sampling data, and Landsat overpass date used for chlorophyll model development.

Location	Station	chl-*a* (μg l^{-1})	Sample date	Landsat date	Difference (days)
Jordan Lake	CPF055C	43	15 May 2013	14 May 2013	1
Jordan Lake	CPF055D	38	15 May 2013	14 May 2013	1
Jordan Lake	CPF055E	24	15 May 2013	14 May 2013	1
Jordan Lake	CPF055E	16	19 May 2014	17 May 2014	2
Jordan Lake	CPF055C3	11	19 May 2014	17 May 2014	2
Jordan Lake	CPF086F	38	19 May 2014	17 May 2014	2
Jordan Lake	CPF086C	48	19 May 2014	17 May 2014	2
Jordan Lake	CPF055C	72	5 August 2014	5 August 2014	0
Jordan Lake	CPF055D	65	5 August 2014	5 August 2014	0
Jordan Lake	CPF086F	32	25 August 2014	21 August 2014	4
Jordan Lake	CPFMC04	44	25 August 2014	21 August 2014	4
Jordan Lake	CPF081A1B	64	10 Sept 2014	6 Sept 2014	4
Jordan Lake	CPM087D	45	22 Sept 2014	22 Sept 2014	0
Watson Reservoir	WR	10	8 May 2015	10 May 2015	2
Gardiner Pond	GP	6	8 May 2015	10 May 2015	2
St Mary's Pond	SMP	8	8 May 2015	10 May 2015	2
Sisson Pond	SP	66	29 June 2015	25 June 2015	4
Nelson Pond	PP	71	14 July 2015	11 July 2015	3
Nonquit Pond	NP	7	12 August 2015	12 August 2015	0
St Mary's Pond	SMP	147	24 August 2015	28 August 2015	4

Table 4

NCDENR and RIDEM stations, sampling data, and Landsat overpass date used for model validations.

Location	Station	chl-*a* (μg l^{-1})	Sample date	Landsat date	Difference (days)
Jordan Lake	CPF087B3	23	15 May 2013	14 May 2013	1
	CPF08880				
Jordan Lake	A	17	15 May 2013	14 May 2013	1
Jordan Lake	CPF086F	35	15 May 2013	14 May 2013	1
	CPF081A1				
Jordan Lake	C	31	15 May 2013	14 May 2013	1
Jordan Lake	CPF086C	48	19 May 2014	17 May 2014	2
Jordan Lake	CPFMC02	46	19 May 2014	17 May 2014	2
Jordan Lake	CPF086F	25	7 August 2014	5 August 2014	2
Jordan Lake	CPF087B3	32	7 August 2014	5 August 2014	2
Gardiner Pond	GP	6	6 May 2015	8 May 2015	2
Nelson Pond	PP	16	6 May 2015	8 May 2015	2
Gardiner Pond	GP	22	12 August 2015	12 August 2015	0
South Easton Pond	SEP	38	12 August 2015	12 August 2015	0
Nelson Pond	PP	52	12 August 2015	12 August 2015	0
Watson Reservoir	WR	12	12 August 2015	12 August 2015	0
Sisson Pond	SP	55	12 August 2015	12 August 2015	0

Table 5

Summary of statistical parameters used to evaluate the effectiveness of selected chlorophyll-*a* models based on several approaches and regression analysis.

Approach	*n*	R^2	*r*	RMSE (μg l^{-1})	MAPE (%)	MAE (μg l^{-1})
3-band (λ_1 = 443)	15	0.66	0.81	8.9	33.5	7.0
3-band (λ_1 = 482)	15	0.58	0.76	10.4	40.2	8.5
FLH violet	15	0.52	0.72	14.2	69.5	13.1
FLH blue	15	0.51	0.71	13.2	65.9	12.0
482/562 ratio	15	0.18	0.43	14.6	46.8	13.0
562/482 ratio	15	0.18	0.42	15.8	45.0	13.2
3-band (λ_1=655)	15	0.05	0.23	19.8	102.7	16.9

Table 6

Comparisons of the difference between chl-*a* concentrations predicted using the 3 band algorithm and spectral data not corrected/corrected for aerosol effects using the L-8 SWIR 1 band

Landsat-8 Image	Date	*n*	Average difference (%) between chl-*a* predicted using non-aerosol and aerosol corrected R_{rs}
LC80160352014233LGN00_sr	24 October 2014	599	14.8
LC80160352015028LGN00_sr	28 January 2015	637	16.0
LC80160352015092LGN00_sr	2 April 2015	594	13.2
LC80160352015188LGN00_sr	7 July 2015	258	31.8
Average			18.9